GA–A23965

MODELING OF STOCHASTIC MAGNETIC FLUX LOSS FROM THE EDGE OF A POLOIDALLY DIVERTED TOKAMAK

by
T.E. EVANS, R.A. MOYER, P. MONAT

JUNE 2002

DISCLAIMER

GA–A23965

MODELING OF STOCHASTIC MAGNETIC FLUX LOSS FROM THE EDGE OF A POLOIDALLY DIVERTED TOKAMAK

by
T.E. EVANS, R.A. MOYER,* P. MONAT*

This is a preprint of a paper to be submitted for publication in *Physics of Plasmas.*

*Center for Energy Research, University of California, San Diego, La Jolla, California

Work supported by
the U.S. Department of Energy
under Contract No. DE-AC03-99ER54463
and Grant No. DE-FG03-95ER54294

GA PROJECT 30033
JUNE 2002

ABSTRACT

A field line integration code is used to study the loss of edge poloidal magnetic flux due to stochastic magnetic fields produced by an error field correction coil (C–coil) in DIII–D [J.L. Luxon, Nucl. Fusion **42,** 614 (2002)] for various plasma shapes, coil currents and edge magnetic shear profiles. We find that the boundary of a diverted tokamak is more sensitive to stochastic flux loss than a nondiverted tokamak. The C–coil has been used to produce a stochastic layer in an ohmic diverted discharge with characteristics similar to those seen in stochastic boundary experiments in circular limiter ohmic plasmas, including: (1) an overall increase in recycling, (2) a broadening of the recycling profile at the divertor, and (3) a flattening of the boundary profiles over the extent of the stochastic layer predicted by the field line integration code. Profile flattening consistent with field line integration results is also seen in some high performance discharges with edge transport barriers. The prediction of a significant edge stochastic layer even in discharges with high performance and edge radial transport barriers indicates that either the self-consistent plasma response heals the stochastic layer or that edge stochastic layers are compatible with edge radial transport barriers.

1. INTRODUCTION

High performance Advanced Tokamak (AT) operation (high $\beta_n H$) will require some form of control over locked, resistive wall, and neoclassical tearing modes [1]. A leading approach in present day devices is the use of external magnetic field coils designed to null the dominant magnetic field perturbation in the plasma core that interacts with these modes. In addition to resistive wall mode and locked mode control coils, a variety of externally driven radial magnetic field perturbation δb_r sources are known to exist in tokamaks. Some have been modeled or studied experimentally although a detailed knowledge of the actual source distributions can typically only be inferred from sparsely populated measurement sets. These include so-called error fields [2,3], fields from tearing modes [4], and topological noise spectra which account for perturbations from small random displacements integrated over the entire field coil ensemble of the device [5]. Additionally, many tokamaks also have nonaxisymmetric perturbation coils specifically designed to create stochastic or ergodic boundaries [6–8]. In circular and low elongation limiter tokamaks, stochastic boundary layers have been used to alter the edge T_e profiles, modify the impurity transport and increase the edge radiation [7,9]. On the other hand, relatively little experimental or theoretical information is available for understanding the effects of edge stochastic layers in moderately elongated, poloidally diverted, neutral beam heated tokamaks.

In DIII–D [10], a series of coil designs ($n=1$, C–coil, [3] and I–coil) have been or are being implemented to enhance core plasma performance by nulling a presumed field error at the $q=2$ surface in order to reduce locked mode effects and the onset of resistive wall modes. Experimentally, it is found that properly phased DIII–D C–coil currents ranging between 6–10 kA-turns significantly reduce the plasma effects associated with error fields and topological noise near the $q=2$ surface. Since the C–coils are used on essentially all DIII–D discharges to control core modes, it is important to understand the impact of these coils on the boundary and scrape-off layer plasma. In this paper, we model the effect of these core mode control coils on the edge magnetic topology and compare the modeling results to experimental measurements.

We present vacuum field line integration results that elucidate the impact of the DIII–D C–coil on the plasma pedestal and divertor separatrix region. Simulation results showing the fractional flux loss $\delta\psi_\ell = \delta\psi_{lcfs}/\psi_{ns}$ as a function of magnetic perturbation strength δb_r, where $\delta\psi_{lcfs}$ is the poloidal flux at the perturbed last closed flux surface and ψ_{ns} is the normalized flux at the unperturbed separatrix, has a complex dependence on the plasma shape

and the edge safety factor profile $q(\psi)$. To fully understand the structure of ψ in any experiment, the combined effects of each significant source of δb_r along with the response of the plasma to these sources must be modeled. For C–coil currents above the typical locked mode correction range, $\delta\psi_\ell$ should be dominated by δb_r from the C–coil rather than from δb_r due to other sources. Under most experimental conditions, C–coil currents of about 30%–50% the maximum 20 kA-turns design value are sufficient to minimize the plasma effects due to error fields and other intrinsic external sources. This suggests that these sources play a correspondingly smaller role in the plasma response at the highest C–coil currents unless strong nonlinear effects due to the plasma response are involved. In this paper, we show that the DIII–D C–coils are predicted, by vacuum magnetic field line integration, to lead to significant stochastic magnetic flux loss from the pedestal and separatrix region at typical operating plasma conditions and coil currents. Comparisons with the level of stochastic magnetic flux loss for nondiverted, inner wall limited (IWL) DIII–D discharges at the same δb_r strength demonstrate that diverted configurations are more sensitive to break up of the axisymmetric flux surfaces in the boundary than nondiverted discharges. Although this sensitivity can be considered a limitation of diverted tokamak configurations, it also provides a possible mechanism for controlling the pedestal region (pedestal height and the concomitant core plasma confinement; edge stability and ELM behavior, density control and helium exhaust, and impurity penetration).

2. BACKGROUND

The C–coil is comprised of six midplane saddle loops spanning $\pi/3$ radians toroidally with a vertical height of 1.6 m. Each loop is positioned at a major radius $R_c = 3.2$ m while the vacuum vessel wall is located at $R_w = 2.35$ m and the plasma center is at $R_0 = 1.67$ m. Each loop has four turns and is designed to carry a maximum current of 5 kA. Toroidally opposing coil pairs are wired in series with antiparallel phases creating a predominantly $n = 1$ toroidal perturbation spectrum with poloidal mode numbers (m) of significant amplitude ranging from $m = 1$ to 6 . On the $q = 2$ surface, the C–coil mode spectrum peaks at $m:n$ = 1:1 with $\delta b_{r,m:n} = \delta b_{r,1:1} = 8.6$ G at full C–coil current I_c = 20 kA-turns. The $m:n$ = 2:1, 3:1 and 4:1 coil components scale roughly as $\delta b_{r,m:1}$ = (11.5–2.8 m) G while $\delta b_{r,5:1} = \delta b_{r,6:1} \approx 0.5$ G [3]. Allowing for a $(r/R_c)^{m-1}$ fall off of $\delta b_{r,m:n}$, the dominant edge resonant modes ($4 \le m \le 6$) have amplitudes of approximately 0.7–1.0 G in the pedestal region at full C–coil current. The total radial magnetic field from the C–coils is 52 G at the outer midplane unperturbed separatrix with the full coil current. The currents in the three $n = 1$ C–coil pairs are controlled independently with bipolar power supplies that typically run in feedback mode referenced to the current in the poloidal and toroidal field coils. Thus, as the plasma shape changes during a discharge, the current in the C–coil changes. The location of the coils is shown in Fig. 1 relative to the DIII–D vacuum vessel and the axisymmetric flux surfaces of a typical double-null (DN) divertor plasma equilibrium.

The C–coil perturbation is modeled with a field line integration code, TRIP3D, using 20 straight line filaments per loop. The vector field $\vec{b}_c$ from each filament at each point along a field line trajectory is calculated using a Biot-Savart algorithm. The TRIP3D code has been adapted to the DIII–D flux surface geometry from the TRIPND code which was used to model resonantly perturbed circular plasmas in Tore Supra [5] and other nondiverted tokamaks with ergodic limiter and ergodic divertor coils [9]. In TRIP3D, the unperturbed plasma equilibrium vector field $\vec{b}_e$ at each point is obtained from an axisymmetric Grad-Shafranov plasma equilibrium solver, the EFIT code [11], which is constrained by experimentally measured magnetic flux data. The TRIPND and TRIP3D codes are basically similar to field line integration codes used on other tokamaks and stellarators, *e.g.*, the GOURDON code [12], the FLOC code [13] and the

MASTOC code [14]. They integrate a set of first-order cylindrical (R,ϕ,z) magnetic (b_R,b_ϕ,b_z) differential equations of the form:

$$\frac{\partial R}{\partial \phi} = \frac{Rb_R}{b_\phi}; \quad \frac{\partial z}{\partial \phi} = \frac{Rb_z}{b_\phi} \quad , \tag{1}$$

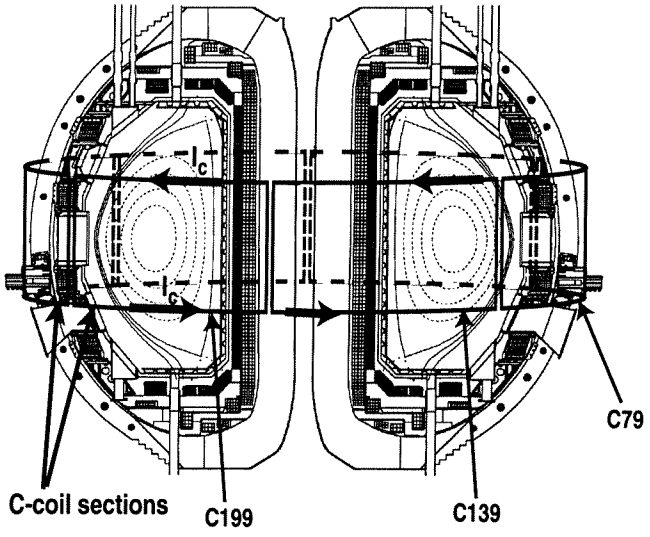

Fig. 1. Cutaway view of the DIII–D device showing the location of the six C–coil segments around the outer midplane of the device. Contours of constant poloidal magnetic flux ψ for a representative axisymmetric DN divertor equilibrium obtained from EFIT are shown.

using a standard Runge-Kutta initial value algorithm with a variable integration step size. Field lines may be integrated starting from any initial point in the plasma and followed in either direction toroidally until their length exceeds a user specified limit or they strike a plasma facing surface.

The backbone of the TRIP codes is made up of four basic elements: the main TRIP program that drives groups of field line integrations based on a set of user prescribed initial conditions, the TRACER algorithm that manages the integration of individual lines and stores the R,ϕ,z position and b_R,b_ϕ,b_z magnetic data in external files, the single step RKFS Runge-Kutta integrator algorithm, and the DFLT magnetic field interrogator algorithm. The integration step size in the toroidal direction, $\Delta\phi$, is set by the user to be small compared to the scale length of the magnetic structures of interest, typically of order 20 to 40 mrad for small islands and stochastic regions. At each step along the integration path, the RKFS algorithm calls DFLT and obtains b_R,b_ϕ,b_z from all the sources specified by the user. The perturbation source fields are

calculated at each integration step as opposed to being interpolated on a grid as is sometimes done in other field line integration codes. While this is computationally more intensive, it provides the accuracy needed to follow field lines over longer distances required for modeling stochastic layers. The difference in the two versions of the TRIP code resides primarily in the model of the unperturbed axisymmetric magnetic equilibrium. In TRIPND, current sources used to model the poloidal and toroidal fields are simulated with circular filamentary loops. Elliptic integrals are used to evaluate the magnetic fields from the individual circular loops. Multifilament plasma current loops are distributed to give realistic safety factor $q(\psi)$ profiles with circular or slightly elongated flux surfaces and small Shafranov shifts. Circular poloidal and toroidal field coils are modeled with groups of circular loops such that the sensitivity of the equilibrium to small nonaxisymmetric shifts and tilts of the coils can be easily evaluated [5]. All calculations in the TRIP codes are done using double precision FORTRAN 90 algorithms.

The TRIP3D code is specifically designed to model elongated flux surfaces in poloidally diverted plasmas, such as DIII–D, by extracting axisymmetric fields from EFIT EQDSK equilibrium files [11]. In addition to providing an accurate representation of the flux surfaces due to external shaping coils, EFIT solutions account for the MHD effects of plasma pressure and current profile distributions on the magnetic equilibrium (*e.g.*, Shafranov shift) and are constrained by experimental magnetic and current profile data on DIII–D. These capabilities are essential for accurately modeling high $\beta_n H$ advanced tokamak plasmas. In TRIP3D, the EFIT equilibrium fields and poloidal fluxes ψ are specified on a 129×129 grid and a bi-cubic spline algorithm is used to evaluate the field between grid points. Extensive numerical tests have been carried out to determine if small nondivergence free field components, introduced by the finite EFIT grid and the spline algorithm, lead to significant errors in the field line integration results. By evaluating fixed points of perturbed and unperturbed trajectories, we find that simulations involving as many as 400 toroidal transits, or about 72,000 toroidal integration steps each of 35 mrad, remain within a 10^{-4} m by 5 mrad rectangle centered on the fixed point in the Poincaré plane. Thus, the uncertainty is about an order of magnitude less than that required for the studies presented in this paper.

We investigate the sensitivity of the axisymmetric equilibria of poloidally diverted discharges with one [lower or upper single null (LSN) or (USN)] or two (double) poloidal magnetic field nulls (divertor X–points) relative to an inner wall limited (IWL) case with no X–points as shown in Fig. 2. The discharge parameters, flux surface shapes, and edge plasma profiles (n_e, T_e, T_i) used here were specifically matched for comparing L–H transition physics among the LSN, USN and DN shapes. The primary plasma parameters for these discharges were: I_p = 1.0 MA, B_ϕ = 2.1 T, $n_e = 2.5\times10^{19}\,\mathrm{m}^{-3}$ and $\kappa = 1.7$ (elongation). Much of the previous

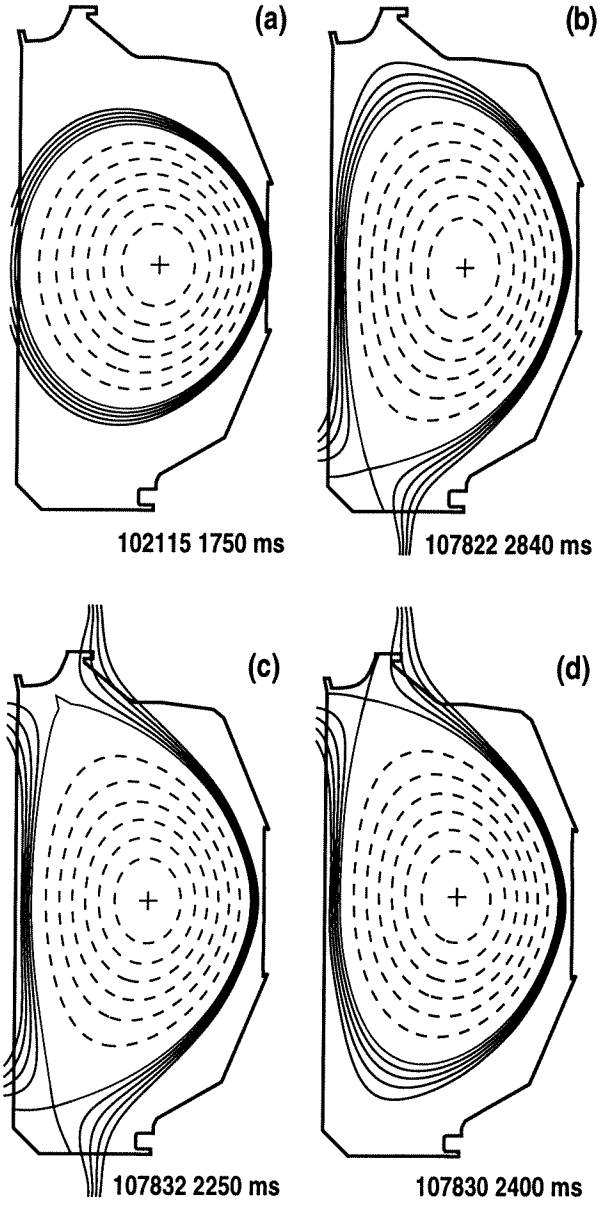

Fig. 2. The unperturbed, axisymmetric equilibria calculated by EFIT for this study, including: (a) IWL, (b) LSN, (c) DN, and (d) USN divertor configurations.

work on stochastic boundary effects in tokamaks has been performed in circular or low elongation ($\kappa \approx 1.0-1.2$) limiter discharges similar to our IWL case. We specifically chose the IWL case to make contact with previous experimental stochastic boundary results and field line modeling work. The primary plasma parameters for this discharge were: I_p = 0.9 MA, B_ϕ = 1.6 T, $n_e = 4.3\times10^{19}\,\mathrm{m}^{-3}$ and $\kappa = 1.2$. The X–points in the diverted discharges lead to higher values of safety factor $q(\psi)$ and magnetic shear $s(\psi)$ in the boundary with respect to the IWL case as shown in Fig. 3. These variations in $q(\psi)$ and $s(\psi)$ for the diverted discharges provide

additional low order resonant surfaces that are more closely spaced than in the IWL. This results in an increased sensitivity of diverted configurations to the break-up of the axisymmetric equilibrium flux surfaces and larger stochastic magnetic flux losses in most cases, a feature first reported by Skinner *et al.* [15]. We also note that the vertical position of the magnetic axis for the single null shapes ranged from $z_{mag} = -0.05$ m for the LSN to $z_{mag} = 0.03$ m for the USN while the DN case had $z_{mag} = 0.00$ m and the IWL case had $z_{mag} = -0.04$ m. These differences in z_{mag} can result in a small variation of the poloidal mode spectrum from fixed external perturbations such as the C–coil, which is centered at $z = 0$ m. Therefore, they can have small but noticeable effects on the stochasticity and magnetic flux loss as discussed below.

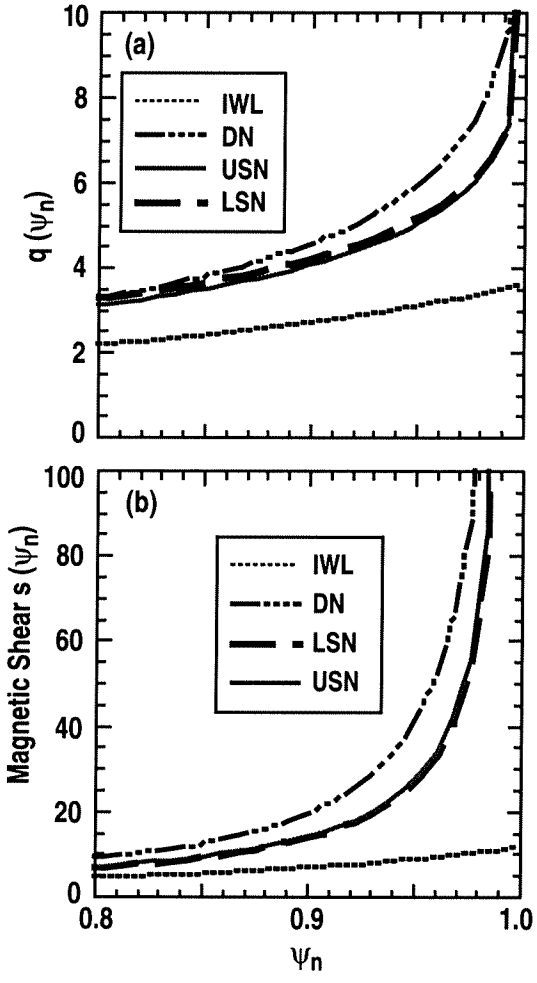

Fig. 3. (a) Edge safety factor $q(\psi)$ and (b) magnetic shear $s(\psi)$ profiles for the IWL, lower and upper SN and DN divertor discharges used in this study. Note that the shear profiles $s(\psi)$ are identical for the LSN and USN shapes.

3. FIELD LINE INTEGRATION RESULTS

We focus on the region just inside the unperturbed divertor separatrix, the so-called "pedestal" region, which is usually bounded in DIII–D by $0.7 < \psi_n < 1.0$. This is typically equivalent to a minor radius r at poloidal angle $\theta = 0$ (the outboard midplane) between 0.5–0.65 m. When viewing the field line integration results on a rectangular Poincaré plot, it is convenient to show the data using a toroidal r,θ,ϕ coordinate system, rather than normalized flux coordinates because fixed structures such as the vessel wall and divertor or plasma facing components and fixed experimental measuring points are not altered by changes in the plasma equilibrium. The r,θ coordinates of each field line intersection with a $\phi = const.$ plane are displayed on the Poincaré plot after each toroidal transit. Since we are often interested in the proximity of magnetic islands to experimental measurement points, we show these Poincaré plots at $\phi = 2\pi/3$, the toroidal angle of the Thomson scattering system, as in Fig. 4. In addition to the field line data, the Poincaré plots show the DIII–D vacuum vessel wall and divertor structures (solid blue line), the unperturbed last closed flux surface or separatrix (magenta) and the positions of the Thomson scattering measurement points (represented by the black "+" symbols in these figures). The field line integration results displayed in the Poincaré plots consist of a single stochastic field line that is launched inside the unperturbed separatrix, crosses the separatrix and strikes a plasma facing material surface (green) and an inner region of closed flux surfaces (red with remnant islands in blue dots). We refer to field lines that cross the unperturbed separatrix from the inside and hit material surfaces as "open" stochastic field lines. Although many open field lines are calculated for each discharge shape and coil current, we show only one open field line in these figures to illustrate behavior of the line and the extent of the region it visits. We typically choose to show the open field line that wanders across the largest inner flux volume.

In general, the topology of the field lines in the stochastic region is quite complex. For example, we usually find both open and closed stochastic lines as well as multiply and singly periodic lines with a range of helical structures (primary and satellite remnant islands) in the pedestal region. In Fig. 4(a), we show an IWL discharge and in Fig. 4(b) an USN discharge. The open stochastic field line shown in these plots is the innermost field line found by probing the magnetic structure with the TRIP3D code from deep within the closed field line region (*i.e.*, well inside the inner radius of the pedestal) out to the unperturbed separatrix. When probing the magnetic structure, we start field lines at $\theta = 0$ with $r = r_{sep} - j\Delta r$ where $j = 0 \rightarrow j_{\max}$,

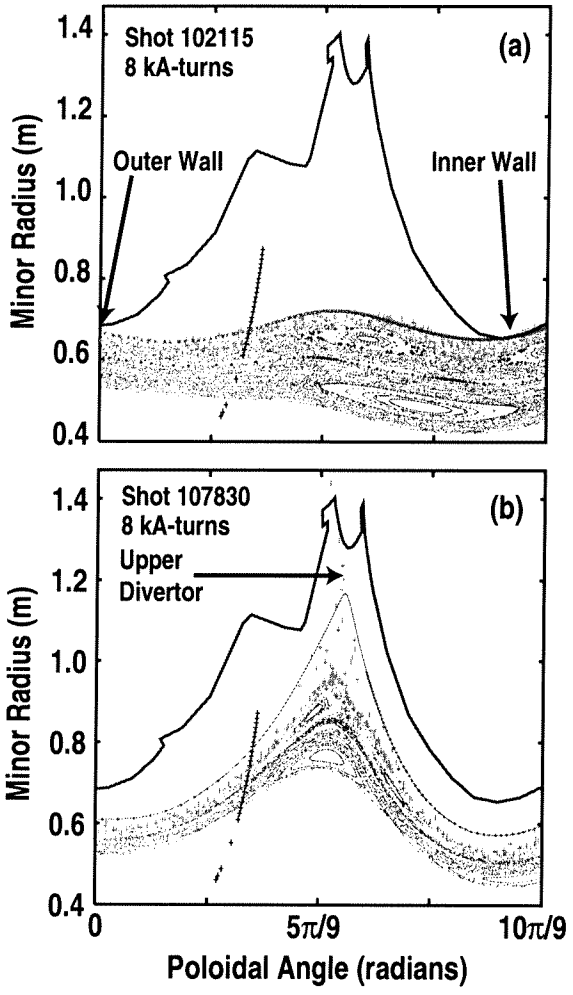

Fig. 4. Rectangular Poincaré plots at a toroidal angle $\phi = 2\pi/3$ for (a) the IWL (102115 with 8 kA-turns) and (b) the USN (107830 with 8 kA-turns) discharges. The colors show, respectively: (blue solid line) the vessel wall; (magenta *) the unperturbed separatrix; (green +) a single stochastic field line that leaves the vessel; (red dots) confined field line trajectories; (blue dots) remnant island flux surfaces; and (black crosses) the Thomson scattering measurement points in the poloidal plane at $\phi = 2\pi/3$.

$\Delta r = 0.5$ mm, $300 \le j_{\max} \le 400$ and r_{sep} is the unperturbed separatrix radius at the outer midplane ($\theta = 0$). For each j corresponding to an open field line, we find a radial minimum $r_{\min}^{open}$ and calculate a displacement $\delta r = r_{sep} - r_{\min}^{open}$. Open stochastic field lines are defined as those lost to a plasma facing surface before making 400 toroidal transits in the forward or reverse B_ϕ direction. After finding δr for each open field line, we choose the maximum displacement and map this into poloidal magnetic flux space in order to calculate the poloidal magnetic flux loss $\delta\psi_\ell$ for each plasma discharge shape and C–coil current. All the field lines studied in these

simulations were followed for either 400 toroidal revolutions or until they hit a plasma facing surface. In most high performance DIII–D pedestal plasmas, this exceeds the parallel electron collisional mean-free path length, so longer field lines are not considered an important factor for understanding parallel thermal particle losses. We have modeled the vacuum magnetic field line trajectories by using both the measured C–coil currents for a particular experimental discharge (see Section IV below) and by scaling the C–coil currents over the full operating range to study the field line behavior for a particular plasma equilibrium. For the scaling studies discussed in this section, we fix the amplitude of each coil to be either $\pm I_c$ and set the phase such that three adjoining loops (c79, c139 and c199 as shown in Fig. 1) are all positive while the opposing loops are all negative. We then vary the coil current between 0 and 20 kA-turns in order to study $\delta\psi_\ell$ as a function of I_c and plasma shape.

The IWL case, shown in Fig. 4(a), has relatively good flux surfaces across the outer 0.10–0.12 m of the plasma with rather large $m:n=3:1$ and 2:1 islands residing in this region. In this case, $\delta\psi_\ell$ is of order 4% but as the current is increased from approximately 8 to 20 kA-turns, these two island chains break up and the outer flux surfaces are lost across the entire region. The USN case for 8 kA-turns, Fig. 4(b), shows that the flux surfaces traversed by a single stochastic field line (green) cover a region which is about 0.06 m inside the unperturbed separatrix (magenta) and that this field line is lost to the upper divertor target plate region along the unperturbed strike point.

In the USN case, Fig. 4(b), the inner most stochastic field line lost to the divertor completes 353.3 toroidal and 74.3 poloidal revolutions with an average $q(\psi)$ of about 4.8. This field line was started at $\phi=2\pi/3$, $\theta=0$, with a minor radius $r_{\min}$ = 0.561 m and hit the outer target plate in the upper divertor ($\theta\approx 3\pi/5$) at $\phi=4\pi/3$. For this discharge, the unperturbed separatrix ($\psi_{ns}\equiv\psi_n=1$) at $\theta=0$ is located at r_{sep} = 0.609 m, corresponding to a maximum δr = 0.048 m or a flux loss $\delta\psi_\ell$ = 0.125. Assuming the field lines behave diffusively, this implies a stochastic field line diffusion coefficient, $D_{st}=\delta r^2/2L$, of 2.9×10^{-7} m where L = 3987 m is the field line length. Clearly, other field lines in the region have a variety of lengths and radial displacements so an ensemble average over N field lines:

$$\langle D_{st}\rangle = \frac{1}{N}\sum_{j=1}^{N}\delta r_j^2/2L_j \quad , \tag{2}$$

in the limit as $N\rightarrow\infty$ provides a more accurate estimate of the average diffusive-like property of the stochastic region. Using only those field lines lost before exceeding an average parallel electron collisional mean-free path length and choosing 36 field lines initiated at 6 toroidal

angles, covering the entire stochastic layer, we find $\langle D_{st} \rangle = 6.9 \times 10^{-8}$ m for the case shown in Fig. 4(b) with I_c = 8 kA-turns. While some field lines deep within the stochastic flux loss region have relatively large values of D_{st}, the average diffusive-like behavior of stochastic layer is dominated by field lines in the outer few centimetres of the layer just inside the unperturbed separatrix. Thus, the effective radial diffusion coefficient D_r across the stochastic layer, for collisionless 1 keV electrons, is approximately 0.9 m^2/s where $D_r = \langle D_{st} \rangle V_{th}$ and V_{th} is the parallel electron thermal velocity. This compares to a radial diffusion coefficient due to turbulent transport of approximately 1 m^2/s in DIII–D [16]. Using a quasi-linear estimate for field line diffusion [17] with an elongation of 1.7 and I_c = 8 kA-turns, we obtain $\langle D_{st}^{QL} \rangle = 4.2 \times 10^{-8}$ m. As shown in Fig. 4(b) the stochastic region due to the C–coil primarily involves the 4:1, 5:1, and 6:1 resonant surfaces so we have included only those $\delta b_{r,m:n}$ harmonics in the calculation of $\langle D_{st}^{QL} \rangle$. While $\langle D_{st} \rangle$ and $\langle D_{st}^{QL} \rangle$ agree reasonably well, the field line data from TRIP3D suggest that the radial displacement of individual field lines is not particularly well characterized by a diffusive Gaussian random process. Nevertheless, $\langle D_{st} \rangle$ is a useful quantity when comparing simulation results for various discharge shapes and C–coil currents.

For the USN case shown in Fig. 4(b), most of the field lines in the region $0.88 < \psi_n < 1.0$ terminate on the upper-outer divertor target near the strike point. Nevertheless, there are some field lines in the stochastic region that remain closed inside partially destroyed remnant islands. The detailed structure of the stochastic region is quite complex. For example, most of the open field lines are focused on the divertor target plates very near the upper outer strike point but there are also some field lines that intersect the divertor target significantly far from the strike point. In general, these differences are not easily quantified as the simulation parameters are changed. To better understand the behavior of $\delta\psi_\ell$ with plasma shape, $s(\psi)$ and I_c detailed modeling of each of the four DIII–D discharges shown in Fig. 2 was carried out using TRIP3D. This set of equilibrium shapes span most of the standard experimental configurations used in DIII–D and provides a representative range of $s(\psi)$ profiles. Figure 5 shows how $\delta\psi_\ell$ scales with I_c in each case. Note the general trend in diverted shapes toward larger $\delta\psi_\ell$ with each value of I_c compared to the IWL shape. Even at the lower coil currents simulated (I_c = 2 kA-turns) we see that each diverted shape has lost about 1.5% of the edge flux while the IWL case requires about a factor of 3–5 higher coil current for the same flux loss. Thus, at one-tenth full current or $\delta b_r \sim 5$ G (total radial magnetic field at the plasma edge) there is a significant stochastic layer in the diverted shapes. Since the boundary is destroyed primarily by the $m = 5-6$ Fourier components of δb_r, the actual perturbation needed to trigger measurable stochasticity is of order 0.1 G or a $\delta b_{r,5:1}/B_\phi$ of approximately 5×10^{-6}. This perturbation level is significantly lower than that studied by Skinner *et al.* for a poloidally diverted tokamak with low elongation

($\kappa \approx 1.0$) [15].The principal uncertainties in these calculations include: (1) flux is trapped in small remnant island cores which results in an overestimate of the flux loss, and (2) island width effects due to the relative phasing of the island X– and O–points at the outer midplane for a fixed toroidal angle (*e.g.*, the inferred poloidal flux loss will vary with toroidal angle). The latter effect tends to underestimate $\delta\psi_\ell$ somewhat, compensating for the flux trapped in the remnant islands. Numerical tests of the flux loss at six different toroidal locations and measurements of the flux trapped in remnant islands indicate that these two effects combine to give a net uncertainty of ± 0.005 in each $\delta\psi_\ell$ value shown in Fig. 5.

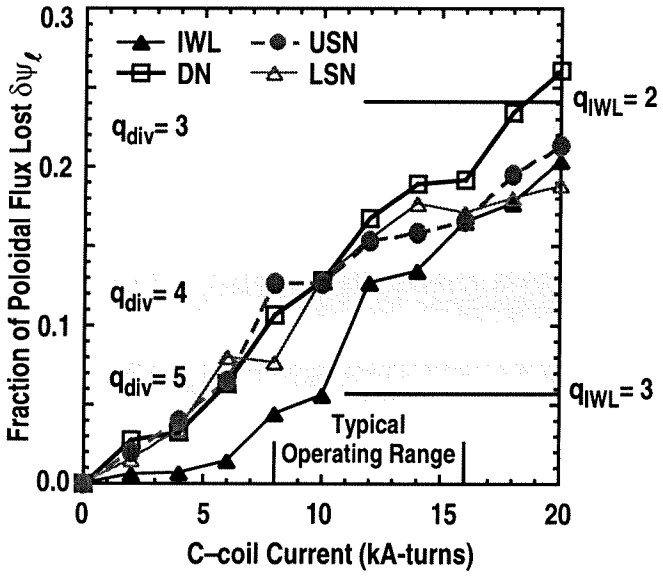

Fig. 5. Scaling of poloidal magnetic flux loss $\delta\psi_\ell$ as a function of C–coil current in the USN, DN, LSN and IWL cases. The radial locations of the resonant q surfaces (in terms of ψ_N) are indicated for the IWL and diverted discharges.

It is clear from Fig. 5 that $\delta\psi_\ell$ is not a simple function of either $s(\psi)$ or I_c as expected from the Chirikov island overlap criteria [18,19] $\sigma_{Ch} = \Delta_m + \Delta_{m+1}/d_{m:m+1}$ for $\sigma_{Ch} \geq 1$ where Δ_m and Δ_{m+1} are neighboring island half widths for $n=1$ resonances and $d_{m:m+1}$ is the distance between the $m:m+1$ resonant surfaces. Here $\Delta_m + \Delta_{m+1} \propto s(\psi)^{-1/2}$ and $d_{m:m+1} \propto s(\psi)^{-1}$ so $\sigma_{Ch} \propto s(\psi)^{1/2}$ and we expect the flux loss $\delta\psi_\ell$ to scale as $s(\psi)^{1/2}$ at constant I_c. In other words, as the magnetic shear increases with constant I_c, the island widths are smaller by $\Delta_m + \Delta_{m+1} \propto s(\psi)^{-1/2}$ while the distance between the islands is correspondingly smaller by $d_{m:m+1} \propto s(\psi)^{-1}$ yielding an increase in the stochasticity that scales as $\sigma_{Ch} \propto s(\psi)^{1/2}$. Note that small variations in the flux loss between the USN and LSN cases at some currents (*e.g.*, 8 kA-turns) are most likely a manifestation of difference in the poloidal mode structure due to

differences in z_{mag} mentioned above. These cases tend to involve rational surfaces with large remnant islands where the uncertainty in the flux loss due to these structures is greatest.

It is of interest to know if the flux loss in diverted plasmas with relatively high magnetic shear can be understood in terms of a simple scaling relationship. A natural choice based on the Chirikov overlap idea discussed above is the square root of the magnetic shear $s(\psi)^{1/2}$. Here we define the weighted average of $s(\psi)$ as:

$$\langle s(\psi)\rangle = \frac{\int_{1-\delta\psi_\ell}^{1} s(\psi_n)\,d\psi_n}{\int_{1-\delta\psi_\ell}^{1} d\psi_n} = \frac{\int_{1-\delta\psi_\ell}^{1} s(\psi_n)\,d\psi_n}{\delta\psi_\ell} \quad . \tag{3}$$

It should be noted that the value of magnetic shear to use in evaluating the Chirikov criterion is not well defined near the separatrix for a realistic divertor tokamak shear profile (parabolic profile versus the constant shear profile used to derive the Chirikov criterion). For example in LSN or USN discharges, when the stochastic layer arises due to overlap of islands formed at the $q = 5$ and $q = 6$ surfaces, the "local" (*i.e.*, at a specific radius) shear varies from 25 to 50 over the extent of the stochastic layer, which demonstrates the ambiguity of choosing a value for $s(\psi)^{1/2}$ scaling. Other definitions for $s(\psi)$were also tried, including (1) the magnetic shear at the outer- or inner-most boundaries of the stochastic layer, and (2) the magnetic shear at the midpoint of the stochastic layer. We found that for wider stochastic layers (higher values of $\delta\psi_\ell$), the definition of magnetic shear used in the Chirikov criterion can significantly affect the results and that the weighted average defined in Eq. (3) gives the best agreement with the predicted $s(\psi)^{1/2}$ scaling. This ambiguity highlights the incompleteness of the Chirikov criterion for evaluation of the onset of global stochasticity in realistic tokamak configurations.

Figure 6 illustrates the relationship between $\delta\psi_\ell$ and $\langle s(\psi)\rangle^{1/2}$ for each I_c where the simulation results (data points) and $\langle s(\psi)\rangle^{1/2}$ scaling at each C–coil current are individually grouped in separate figure frames. The solid lines represent a $\langle s(\psi)\rangle^{1/2}$ scaling of $\delta\psi_\ell$ based on the IWL case; the shaded areas represent the range in the predicted scaling due to the uncertainties in the IWL data. The TRIP3D simulation results are plotted as: filled circles (IWL), open squares (DN), open triangles (USN), and "x" (LSN); the data points represent each of the simulation points from Fig. 5. The error bars indicate uncertainties due primarily to the finite radial spacing of the launched field lines in the simulations and remnant island effects discussed above. The DN case fits a $\langle s(\psi)\rangle^{1/2}$ scaling from the IWL case reasonably well for most values of I_c when the uncertainties in the simulated data are included. On the other hand, the single-null

cases diverge from the $\langle s(\psi)\rangle^{1/2}$ scaling significantly for I_c = 6, 10, 16, 18 and 20 kA-turns. In addition, at low I_c (≤10 kA-turns) the single-null cases have substantially larger $\delta\psi_\ell$ than that predicated by the scaling; while at high I_c (≥12 kA-turns), $\delta\psi_\ell$ is significantly below the predicted values base on the $\langle s(\psi)\rangle^{1/2}$ scaling. Note also the LSN and USN cases can differ significantly (8 and 20 kA-turns), despite the identical $s(\psi)$ profiles [Fig. 3(b)], a clear demonstration that affects other than the shear profile, such as the vertical position of the magnetic axis z_{mag}, are important.

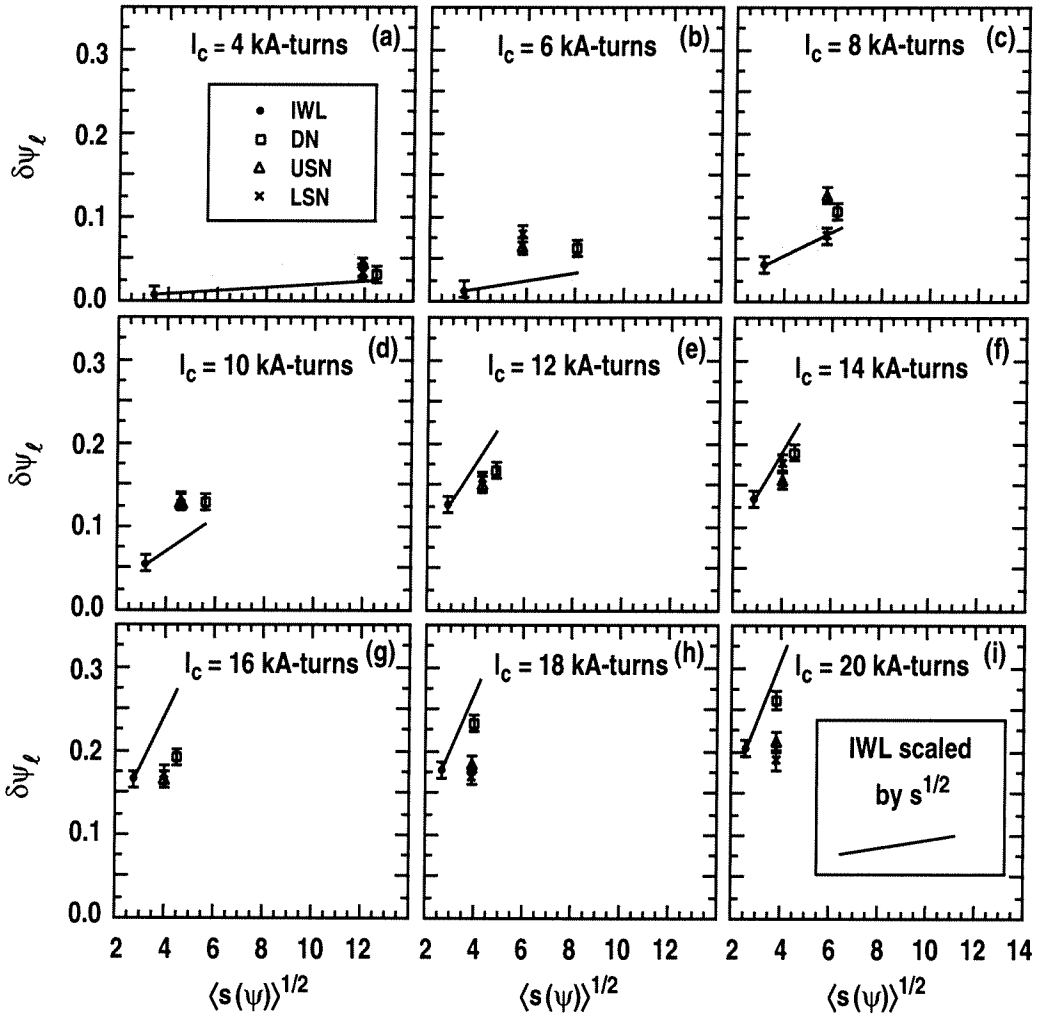

Fig. 6. Comparison of the flux loss $\delta\psi_\ell$ with a $\langle s(\psi)\rangle^{1/2}$ scaling of the IWL case. The results and predictions are grouped by C–coil current I_c in individual frames (a)–(i). The symbols correspond to the simulation results shown in Fig. 5: filled circles (IWL), open squares (DN), open triangles (USN) and "x" (USN). The lines indicate a $\langle s(\psi)\rangle^{1/2}$ scaling of the IWL result, while the shaded areas indicate the range in the $\langle s(\psi)\rangle^{1/2}$ scaling due to the uncertainty in the IWL value of $\delta\psi_\ell$.

4. EXPERIMENTAL IMPLICATIONS OF STOCHASTIC BOUNDARIES IN HIGH POWER POLOIDALLY DIVERTED PLASMAS

Since core mode control coils, such as the DIII–D C–coil, are considered essential for sustaining the highest performance levels in diverted plasmas and will most likely be an essential component of future high performance tokamaks designs, we need to develop a comprehensive understanding of their effects on the core as well as the edge plasma. In addition, there may be significant benefits in being able to control the magnetic topology of the pedestal region independent of that in the core plasma. While many control coil designs are possible, physical constraints and space limitations will most likely make it difficult or impractical to design coils that only perturb the core (*i.e.*, that only have significant $m = 1$, 2 or 3 harmonics) or stochastic boundary coils with only $m > 3$ harmonics. Thus, it is important to better understand how nonideal coils, such as the DIII–D C–coil, affect both the plasma stability and confinement of the core and the edge as well as the magnetic topology of the two regions with various shapes and with increasing input power. Dedicated experiments have been carried out in DIII–D specifically for this purpose. Because of the difficulty involved in isolating individual coil effects during high-power diverted discharges, experiments were first done in ohmic DN diverted plasmas with the currents in the C–coils phased to minimize the effects of the coil on the core plasma. In this section, we discuss results from these experiments and present TRIP3D modeling for several cases of interest. We conclude this section with a discussion of high performance discharges that have features similar to those in ohmic discharges with stochastic boundaries and contrast these to high performance cases where plasma effects may be masking the edge stochastic topology.

The evolution of several key plasma parameters, taken in an ohmic discharge with various C–coil currents, is shown in Fig. 7. During the first 2500 ms of this discharge, the C–coil is actively controlled using the standard DIII–D locked-mode feedback algorithm. At 2500 ms, the C–coil currents are changed in such a way as not to significantly alter the profiles at the $q = 2$ surface where so-called locked modes are generally seen. We observe a small transient reduction in the electron density n_e [Fig. 7(a)] and an increase in the lower divertor D_α recycling [Fig. 7(e)] as the C–coil currents assume their new values [Fig. 7(b)] at 2750 ms. The amplitude [Fig. 7(c)] and phase [Fig. 7(d)] of the radial magnetic field measured by a set of locked mode detectors (compensated for direct pickup from the C–coil) indicates a substantial change in the radial magnetic field due to a plasma response. This type of signal is characteristic of a "locked" mode on the $q = 2$ surface but, in this particular case, there is no evidence for such a mode based

on the plasma profiles around the $q = 2$ surface. Instead, we observe a change in the edge plasma profiles that is consistent with formation of a stochastic boundary: (1) T_e and n_e profile flattening locally in the edge; (2) increased recycling consistent with connecting field lines from inside the separatrix to the divertor (Fig. 8 inset); and (3) broadened particle flux profile on the divertor floor inferred from broadening of the D_α profile (Fig. 8).

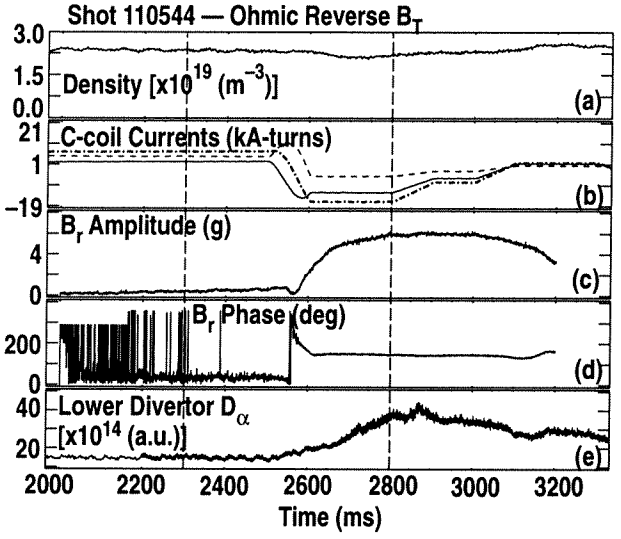

Fig. 7. Plasma response to C–coil change in discharge 110544: (a) line average density, (b) C–coil currents, radial error field (c) amplitude, (d) phase, and (e) divertor D_α recycling near the outer strike point.

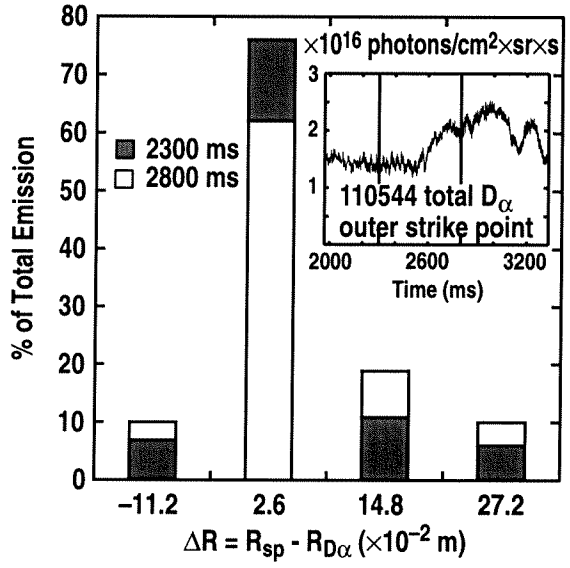

Fig. 8. Broadening of the D_α profile when the stochastic layer is formed. Inset shows the increase in overall recycling. ΔR is the distance of the D_α measuring chord from the strike point.

Figure 8 shows the change in normalized D_α recycling from four chords viewing the lower outer strike point at 2300 ms (shaded) and 2800 ms (white). Each bar represents the local recycling measured by a single chord divided by the total recycling from all four chords (inset). Each chord is referenced to the outer strike point radius (ΔR = outer strike point major radius R_{sp} minus the D_α view major radius $R_{D\alpha}$). Note that although the recycling is still strongly peaked near the outer strike point (ΔR = 2.6 cm) at 2800 ms but the change in the C–coil current reduced the normalized recycling at this location from about 76% to roughly 60% of the total emission. At the same time, the normalized recycling at each of the other observation points increased by roughly 3%–8%. Thus, the recycling profile has broadened, consistent with field line spreading near the strike point while the increase in the overall level of recycling implies that more particles are flowing into the divertor region. While this spreading of the recycling is generally similar to results from circular stochastic boundary experiments, the X–point in this discharge tends to keep the field lines somewhat more "focused" into the divertor region than in nondiverted discharges.

The TRIP3D code was used to model this discharge at 2800 and 2300 ms using the actual C–coil currents and phases shown in Fig. 7(b). At 2800 ms, the unperturbed outer separatrix position from EFIT is $r^{sep}_{mid-out}$ = 0.635 m [Fig. 9(b)]. The solid violet line in Fig. 9 is the DIII–D first wall and the dashed blue line is the unperturbed EFIT separatrix position. The figure shows the field line r,θ positions after each toroidal transit (black, red and green dots) at a toroidal angle $\phi = 2\pi/3$ (the Thomson scattering location: dark blue dots near $\theta = \pi/3$). The field lines are started at $\phi = 2\pi/3$, $\theta = 0$ and 0.5 m < r < 0.635 m in 0.5 mm steps. The black dots are field lines that do not cross the unperturbed separatrix while the red and green dots are those field lines that cross the separatrix and intersect a material surface. Red field lines are integrated in the forward B_ϕ direction and green lines are integrated in the reverse B_ϕ direction. The modeling shows that the C–coil currents and phases at 2800 ms [Fig. 9(b)] produce a much broader stochastic region than those at 2300 ms [Fig. 9(a)]. The width of the stochastic region increases by a factor of 2.5 at the outer midplane between 2300 and 2800 ms, corresponding to 3 and 9 Thomson points at 2300 ms [Fig. 10(a)] and 2800 ms [Fig. 10(b)], respectively, in agreement with the T_e profile changes shown in Fig. 10(c) and 10(d).

The structure of the field lines near the lower divertor X–point indicate that, in addition to those field lines lost very close to the unperturbed inner and outer divertor legs, there are secondary striations further away from the legs at 2800 ms that are not seen at 2300 ms. These secondary striations intersect the divertor about 0.10–0.14 m away from the nominal strike points (both along the inner wall above the inner strike point and outside the outer strike point in the outer scrape-off layer) and indicate a significant broadening of the magnetic flux profiles on the

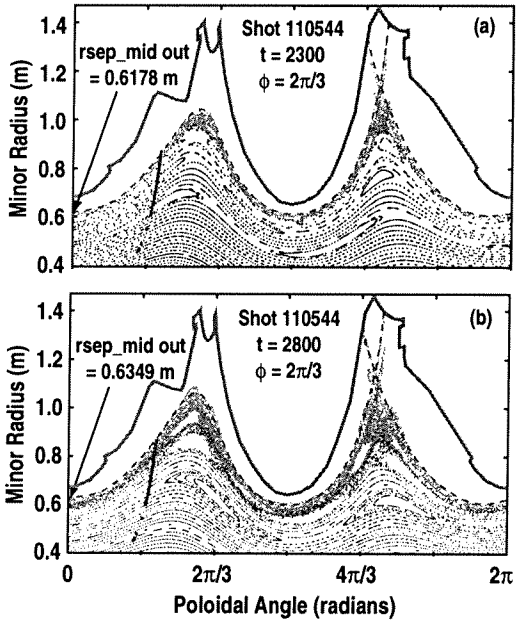

Fig. 9. TRIP3D results for DIII–D discharge 110544 at (a) 2300 ms and (b) 2800 ms. Black dots represent field lines that do not cross the unperturbed separatrix. Red and green dots represent field lines integrated in the forward (red) and reverse (green) B_T direction that intersect a material surface.

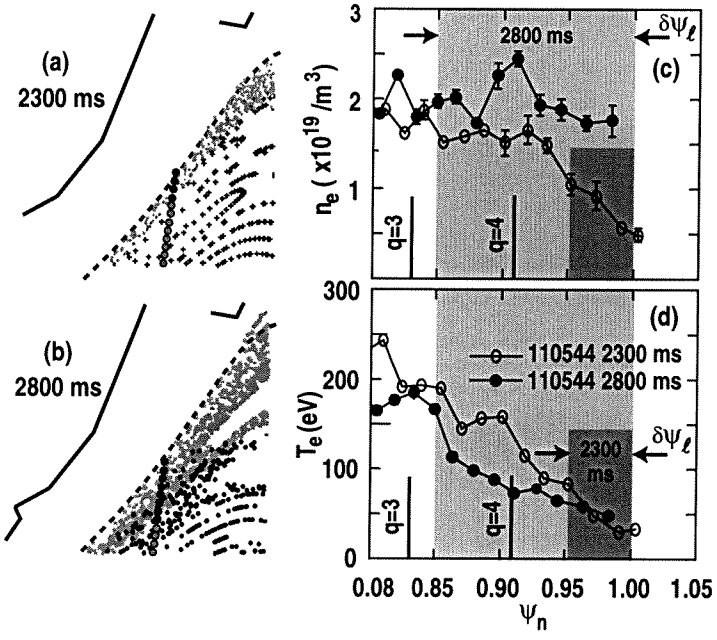

Fig. 10. Expanded view of the field line structure along the Thomson scattering chord at (a) 2300 ms and (b) 2800 ms in discharge 110544. The Thomson scattering points (crosses) are plotted as purple (in) and blue (out) of the stochastic layer. The Thomson (c) density and (d) T_e profiles are plotted at (blue) 2300 ms and (red) 2800 ms. The shaded boxes indicate the predicted extent of the stochastic layer at (light blue) 2300 ms and (light red) 2800 ms. Based on the starting radius of the first field line connecting to a material surface, the width of the stochastic layer is 19 mm (2300 ms) and 44 mm (2800 ms).

divertor targets consistent with a broadening of particle flux profiles seen in the experiments (Fig. 8). The complex structure of the stochastic layer can also be seen in the profile of the parallel connection length L_c of the magnetic field lines to material surfaces (Fig. 11). As one moves into the plasma core, L_c generally increases but there is significant structure. Using the data shown in Fig. 11(a) and Eq. (2) with $N = 44$, we find $\langle D_{st} \rangle = 6.8 \times 10^{-8}$ m in the narrow stochastic layer (*i.e.*, with $\langle |I_c| \rangle \approx 5$ kA-turns at 2300 ms) and $\langle D_{st} \rangle = 6.9 \times 10^{-7}$ m using the data shown in Fig. 11(b) with $N = 60$ for the wider stochastic layer at 2800 ms where $\langle |I_c| \rangle \approx 11$ kA-turns. As discussed above, there is a significant variation in $\langle D_{st} \rangle$ across the stochastic layer with the largest value of $\langle D_{st} \rangle$ found near the inner boundary between the stochastic layer and the core plasma in both cases for discharge 110544. For comparison, the parallel connection length to the divertor target for field lines just outside the separatrix in the unperturbed equilibrium is about 50 m, while the collisional mean-free path varies from 16 to 62 m across the stochastic layer in this discharge.

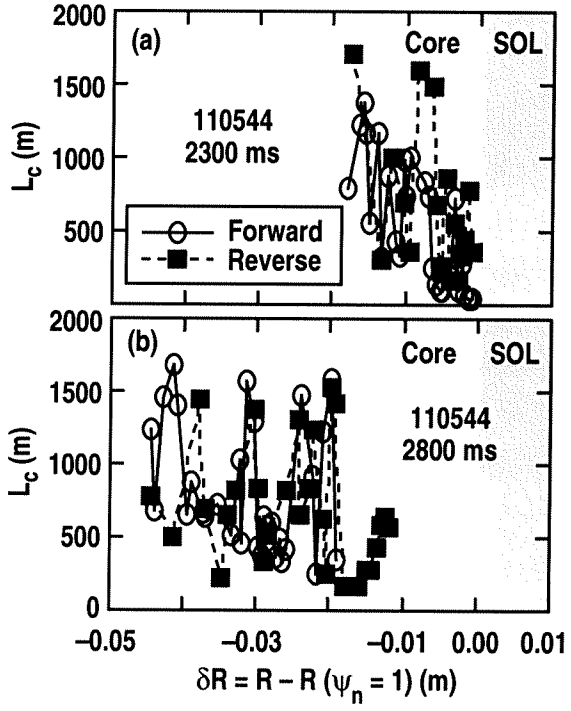

Fig. 11. Field line connection length from outboard midplane ($\phi = 120$ deg) to the vessel wall at 2300 ms (squares) and 2800 ms (triangles). Open symbols correspond to the connection length in the forward B_T direction; solid symbols correspond to the reverse B_T direction.

To date, the limited experimental data available suggest that, at least for *circular limiter ohmically heated discharges*, vacuum magnetic field line integration results are a reasonable quantitative match to the real plasma response as shown in Fig. 12. Our analysis of ohmically

heated DIII–D diverted discharges, such as the one discussed above, also suggest that the edge plasma response has a relatively minor impact on the boundary layer magnetic topology. This would indicate that relatively little or no plasma "self-healing" of the island-stochastic magnetic structure occurs under low power plasma conditions. In high performance DIII–D discharges, however, the additional power flow or momentum input from high-power neutral beam heating might produce a plasma response which significantly heals the island-stochasticity topology via plasma rotation or some other effect. Understanding the self-consistent plasma response is critical for interpreting experimental results for tokamak pedestal and scrape-off layer physics and for developing predictive models of the edge plasma in tokamaks. Such understanding might, in turn, lead to new techniques for controlling the pedestal and boundary of high performance tokamaks.

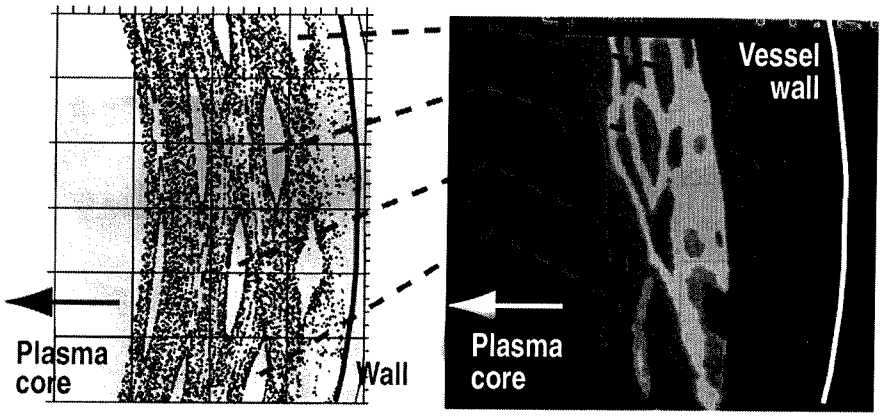

Fig. 12. Comparison of a TRIPND vacuum field line integration simulation (left) with an image of the stochastic layer for an ohmic discharge with 15 kA in the ergodic divertor coils at Tore Supra. The image is a tangential view of total visible light taken near the high field side plasma facing surface. The spatial scales of the image and the simulation are approximately the same. Red dashed lines indicated island remnants within the stochastic layer which are reproduced quantitatively in the simulation (both location and size).

As discussed above, it is often difficult to distinguish between core and boundary effects produced by the C–coil in DIII–D particularly as the power and momentum input is increased. In fact, as the C–coil current is increased in high power plasmas, in an effort to increase the stochasticity of the pedestal region, core effects such as so-called locked and resistive wall modes dominate the behavior of the plasma profiles and effectively mask any edge effects. Nevertheless, some high-power discharge conditions do result in a pronounced flattening of the edge T_e profile and in a transport barrier-like behavior similar to that observed during previous stochastic boundary layer experiments [9,20,21]. Figure 13 shows the pedestal profiles for a

typical "quiescent double barrier" mode (QDB) discharge, an ELM-free H–mode discharge in the DIII–D tokamak [22]. A 3 cm ($0.95 < \psi_{ns} < 1.0$) flat region in T_e [Fig. 13(b)] and a corresponding 4 cm ($0.93 < \psi_{ns} < 1.0$) flat region in the plasma density [Fig. 13(a)] are seen during the QDB phase of this discharge, a result that is typical of QDB discharges with a strong edge harmonic oscillation (EHO) [23]. The lack of ELMs in these discharges appears to be a key ingredient in our ability to observe the edge profile flattening; whereas in ELMing H–mode discharges, the profile flattening appears to be "washed out" by the ELMs.

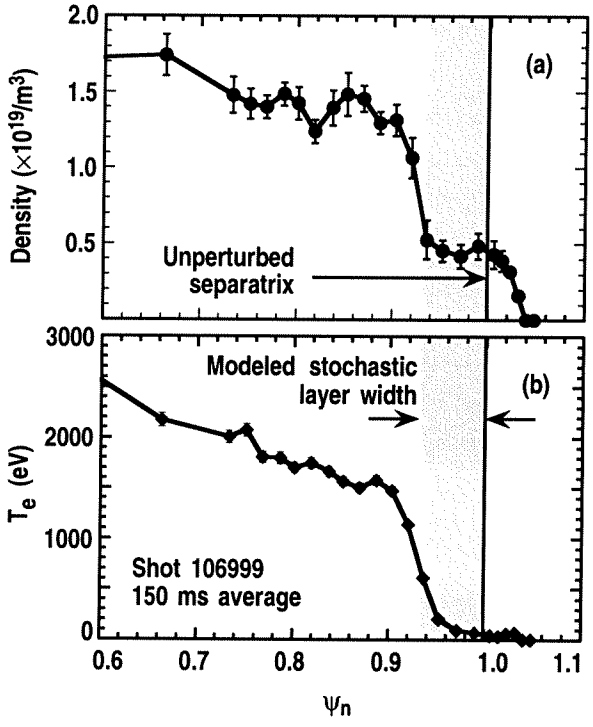

Fig. 13. Plasma density (a) and electron temperature (b) profiles measured by Thomson scattering for shot 106999 (USN) showing flat regions at the edge.

Simulations of this QDB discharge with the actual C–coil currents and phases used in the experiment (I_{c79} = –4.3 kA-turns, I_{c139} = –6.7 kA-turns, I_{c199} = –2.4 kA-turns at t = 2400 ms) produce a 4 cm wide stochastic layer at the location of the Thomson scattering system used to measure the T_e profile. The density profile flattening seen in this case could then result from the combination of an edge stochastic layer (model prediction) and the quiescent H–mode (QH) radial transport barrier (experimentally measured). While this flattening is consistent with the width of the stochastic layer modeled with the TRIP3D code, it has yet to be shown explicitly that these flat profiles are caused by some combination of δb_r fields in the pedestal due to either the C–coil, error fields, or internal modes (such as the magnetic field of the EHO itself). A

definitive proof of the existence of an edge stochastic layer in such a high performance QDB mode discharge would establish the compatibility of edge stochastic layers with high confinement operation. In contrast, definitive proof of the lack of such a stochastic layer would establish the need to better understand the self-consistent plasma response to stochastic field regions.

5. CONCLUSIONS

In conclusion, we have shown explicitly that the boundary of a diverted tokamak is more sensitive to a loss of magnetic flux to the wall by stochastic transport due to resonant radial field perturbations than the boundary of nondiverted tokamaks. As shown in Section III, a total perturbation field $\delta b_r \sim 5$ G is sufficient to produce a stochastic layer width of 1.5% in normalized poloidal flux during diverted discharges whereas about 3–5 time larger perturbations are needed to produce the same flux loss in the IWL case. Since the boundary is destroyed primarily by the $m=5-6$ Fourier component of δb_r, the actual perturbation needed to trigger stochasticity is of order 0.1 G. This level of δb_r is significantly lower than that studied by Skinner *et al.* for a poloidally diverted tokamak with low elongation ($\kappa \approx 1.0$) [15].

This result is qualitatively consistent with a $s(\psi)^{1/2}$ scaling (for suitably chosen s) implied by the Chirikov island overlap model due to the increased levels of magnetic shear in the boundary of diverted tokamaks relative to nondiverted tokamaks, but the details of the flux loss scaling with discharge shape and δb_r suggest that the simple Chirikov island separatrix overlap picture is inadequate for understanding the complex nature of the stochastic flux loss in the boundary of a toroidal confinement device. The $s(\psi)^{1/2}$ scaling does not quantitatively describe the variation in stochastic region width with divertor configuration or perturbation field strength/coil current seen in this field line integration study. In particular, the DN is in rather good agreement for all currents while the SN departs from agreement at both the lowest and highest coil currents.

In some cases, the existence of a stochastic layer just inside the unperturbed separatrix is consistent with experimental observations of T_e profile flattening and a broadening of the divertor recycling profiles such as in ohmic discharges with properly chosen C–coil currents and QDB discharges without ELMs. However, these effects are not always seen for cases that are predicted to have a stochastic edge, leaving the self-consistent plasma response to such stochastic layers and the effects of ELMs as an open question. In circular limiter ohmic discharges, the existing experimental data suggests that the widths and locations of remnant islands embedded in the stochastic region are in good agreement with field line integration results. This result indicates that, at least for those conditions, there is little or no plasma "self-healing" of the stochastic layer.

Successful routine tokamak operation in high confinement regimes with currents in the external magnetohydrodynamic control coils that are predicted to cause stochastic layers of up to 25% of the poloidal magnetic flux, suggests that either the plasma heals the stochastic region (*e.g.*, due to plasma rotation) or that the stochastic layer is compatible with edge (H–mode) transport barriers.. While signatures of stochastic boundary effects have been observed during DIII–D ELM-free improved confinement modes (*i.e.*, QDB discharges such as that shown in Fig. 13), we do not fully understand why these discharges agree relatively well with the predicted widths of the stochastic layer simulated in TRIP3D and ELMing H–modes show no indications of a flattening in the edge T_e profile commonly associated with stochastic layers. This highlights the need to improve our understanding of the self-consistent plasma response to stochastic magnetic field layers in high performance tokamak discharges. With improved understanding, it may be possible to use external coils to control the edge pedestal region, including: edge stability, ELM behavior, pedestal height and width, neutral and impurity penetration and screening, and power flow to plasma facing components.

ACKNOWLEDGEMENTS

We would like to thank D.R. Baker for first pointing out to us the pedestal profile flattening shown in Fig. 13 and suggesting that its features appeared to be very similar to those seen in stochastic boundary layer experiments in limiter plasmas. T.E. Evans would like to thank D. Guilhem for his help in obtaining the tangential visible light image of the magnetic islands shown on the right side of Fig. 12 and F. Allais for his assistance in developing the TOSU6 and TRIPND codes used to calculate the vacuum field magnetic islands shown on the left side of Fig. 12.

This work was supported by the U.S. Department of Energy under Contract No. DE-AC03-99ER54463 and Grant No. DE-FG03-95ER54294.

REFERENCES

[1] M. Okabayashi, J. Bialek, M.S. Chance, *et al.*, Phys. Plasmas **8**, 2071 (2001); A.M. Garofalo, T.H. Jensen, L.C. Johnson, *et al.*, Phys. Plasmas **9**, 1997 (2002).

[2] N. Pomphrey, A. Reiman, Phys. Fluids B **4**, 938 (1992).

[3] J.T. Scoville and R.J. La Haye, *Proceedings of the 14th IEEE/NPSS Symposium on Fusion Engineering, San Diego, 1991* (Institute of Electrical and Electronics Engineers, Inc., Piscataway, 1992) Vol. II, p. 1144.

[4] E. Uchimoto, J.D. Callen, Zuoyang Chang, S.C. Prager, Phys. Plasmas **1**, 648 (1994).

[5] T.E. Evans, *Proceedings of the 18th European Physical Society Conference on Controlled Fusion and Plasma Physics, Berlin, 1991* (European Physical Society, Petit-Lancy, 1991) Part II, p. 65.

[6] K.H. Finken, S.S. Abdullaev, T. Eich, D.W. Faulconer, M. Kobayashi, R. Koch, G. Mank, A. Rogister, Nucl. Fusion **41**, 503 (2001).

[7] Ph. Ghendrih, A. Grosman, and H. Capes, Plasma Phys. Control. Fusion **38**, 1653 (1996).

[8] M.Z. Tokar, Phys. Plasmas **6**, 2808 (1999).

[9] T.E. Evans, J.S. deGrassie, G.L. Jackson, *et al.*, J. Nucl. Mater. **145–146**, 812 (1985).

[10] J.L. Luxon, Nucl. Fusion **42,** 614 (2002).

[11] L. Lao, H. St. John, R.D. Stambaugh, A.G. Kellman, W. Pfeiffer, Nucl. Fusion **25**, 1611 (1985).

[12] A. Kaleck, M. Habler, and T. Evans, Fusion Eng. and Design **37**, 353 (1997).

[13] R.H. Fowler, D.K. Lee, P.W. Gaffney, J. A. Rome, "FLOC – Field Line and Orbit Code for the Study of Ripple Beam Injection into Tokamaks," ORNL/TM-6293 Dist. Category UC-20g (1978).

[14] F. Nguyen, P. Ghendrih, A. Samain, "Calculation of the Magnetic Field Line Topology of Ergodized Edge Zone in Real Tokamak Geometry. Application to the Tokamak Tore Supra through the MASTOC Code," Rep. EUR-CEA-FC-1539, Association Euratom-CEA (1995).

[15] D.A. Skinner, T.H. Osborne, S.C. Prager, W. Park,. Phys. Fluids **30**, 1218 (1987).

[16] R.A. Moyer, J.W. Cuthbertson, T.E. Evans, G.D. Porter, J.G. Watkins, J. Nucl. Mater. **241–243**, 633 (1997).

[17] A.B. Rechester, M.N. Rosenbluth, Phys. Rev. Lett. **40**, 38 (1978).

[18] B.V. Chirikov, Physics Reports **52**, 265 (1979).

[19] A.J. Licthenberg, M.A. Lieberman, *Regular and Stochastic Motion* (Springer-Verlag, New York, 1983) p. 213.

[20] T.E. Evans, M. Goniche, A. Grosman, D. Guilhem, W. Hess, J. Vallet, J. Nucl. Mater. **196–198**, 421 (1992).

[21] M. Becoulet, H. Capes, Ph. Ghendrih, A. Grosman, J. Gunn, G.T. Hoang, J.L. Segui, M. Zabiego, Contrib. Plasma Phys. **40**, 251 (2000); P. Thomas, *Proceedings 29th EPS Conference on Plasma Physics and Controlled Fusion*, Montreux, 2002 (European Physical Society, available on CD-ROM).

[22] K.H. Burrell, M.E. Austin, D.P. Brennan, Phys. Plasmas **8**, 2153 (2001).

[23] K.H. Burrell, M.E. Austin, D.P. Brennan, *et al.*, "Quiescent H–Mode Plasmas in the DIII–D Tokamak," presented at the *8th IAEA Technical Committee Meeting on H–Mode Physics and Transport Barriers, Toki, 2001*, to be published in the Plasma Physics and Controlled Fusion.